



RESEARCH PAPER •

Acta Mech. Sin., Vol. 40, 423122 (2024) https://doi.org/10.1007/s10409-023-23122-x

Influence of chemistry and temperature on mechanical behavior and deformation mechanisms of refractory high-entropy alloys: an integrated simulation-modeling analysis

Jia Li¹, Siwei Ren¹, Bin Liu², Peter K. Liaw³, and Qihong Fang^{1*}

Received March 12, 2023; accepted July 17, 2023; published online September 27, 2023

The equiatomic refractory high-entropy alloys (RHEAs) exhibit the excellent performance at high temperatures, breaking through the upper limits of operating temperatures in the conventional high-temperature alloys. Here, the influences of chemistry and temperature on the deformation mechanisms of the equiatomic MoNbTaW RHEAs are investigated, using the large-scale atomic simulations. According to the microstructure evolution, a microstructure-based constitutive model is established to study the effects of the multiple strengthening mechanisms. The results show the jagged sharp fluctuations of the flow stress with the strain after the strain hardening. The increasing temperature reduces the strain-hardening rate and the amplitude of fluctuations in the flow stress, due to the reduction of the solute concentration for the annealed structure. The deformation twinning plays a certain role in the deformation mechanism in comparison with dislocation, and the local deformation is further accommodated via the dislocation-based plasticity, and amorphous nucleation in the grains. The existence of the ordered structure affects the stress and strain partition dependent upon the mechanical properties. The solid solution strengthening and grain boundary strengthening contribute considerably to the flow stress, and twinning strengthening contributes relatively little to the flow stress. Our atomic simulation and model give valuable insights into the deep understanding of chemistry and temperature related to the deformation behaviour of RHEAs.

Refractory high entropy alloys, Temperature, Short-range ordering, Mechanical properties, Deformation behaviour

Citation: J. Li, S. Ren, B. Liu, P. K. Liaw, and Q. Fang, Influence of chemistry and temperature on mechanical behavior and deformation mechanisms of refractory high-entropy alloys: an integrated simulation-modeling analysis, Acta Mech. Sin. 40, 423122 (2024), https://doi.org/10.1007/s10409-023-23122-x

1. Introduction

With the rapid development of the extreme equipment in the field of high temperature, the performance requirements and demand for elevated-temperature components are continuously increasing [1,2]. However, the currently used superalloys, mainly including Fe-based, Co-based, and Nibased alloys, are at present approaching the upper limits of operating temperatures and stresses [3], which cannot meet

To promote the applications, such as gas turbine, nuclear reactor, and heat exchanger, some reports on RHEAs explore the process-structure-properties relationships by extensively characterizing specific alloy compositions [8-11]. The MoNbTaW RHEA synthesized by vacuum arc melting

¹ State Key Laboratory of Advanced Design and Manufacturing for Vehicle Body, College of Mechanical and Vehicle Engineering, Hunan University, Changsha 410082, China;

² State Key Laboratory of Powder Metallurgy, Central South University, Changsha 410083, China;

³ Department of Materials Science and Engineering, The University of Tennessee, Knoxville 37996, USA

the design requirement of the hot-end components. Therefore, the development of the alternate materials is extremely urgent to operate at elevated temperatures. Recently, the multi-principal elements or refractory high-entropy alloys (RHEAs) could offer a strategy to develop an ideal novel high temperature structure [4-7], due to their excellent mechanical properties.

^{*}Corresponding author. E-mail address: fangqh1327@hnu.edu.cn (Qihong Fang) Executive Editor: Yuli Chen

shows the high hardness of 4.69 GPa owing to strong solid solution strengthening [12]. By high-throughput additive manufacturing and characterization, a model MoNbTaW alloy system is explored for exceptionally high strength at elevated temperature [13,14]. In comparison to pure tungsten, the MoNbTaW RHEA exhibits the increased resistance to irradiation suitable for fusion reactor components [15]. The polycrystalline multi-phase MoNbTaTiW shows a high absolute hardness of 13.89 GPa due to solid solution strengthening and grain boundary strengthening [16]. On the other hand, the dislocation behavior and deformation mechanism in the MoNbTaW RHEA are investigated, using the model and atomic simulation. The effect of chemical shortrange ordering (CSRO) on the energy landscape of screw/ edge dislocation and the screw/edge dislocation mobility are studied in MoNbTaW RHEA over a wide temperature range using molecular dynamics (MD) simulations [17-19]. Using a theory of edge dislocation strengthening in BCC alloys, the strength of MoNbTaW RHEA is controlled by edge dislocations at high temperatures, attributed to large energy barriers for the thermally-activated edge glide [20]. The liquidus temperature and density in RHEAs are calculated using the rule-of-mixtures relations and calculation of the phase diagram approach, for obtaining the weightage of different properties based on their design and application requirements [21].

It is widely known that the MoNbTaW system reported by Senkov et al. [22] in 2010 is a very classic system in the field of RHEAs [23-25]. Here, we try to examine the atomic-scale deformation mechanism from the perspective of modeling and simulation, to further understand the mechanical behavior and improve performance. The understanding and representation at different levels of experiment drive the development of simulation and model to obtain more general rules. It is undeniable that simulation is a very important method to understand the phenomena of the material world. In this study, the deformation behaviours of MoNbTaW RHEA system are considered using an integrated simulation-modeling analysis in terms of microstructure, dislocation type, strain, and stress distribution. The basic mechanical properties are also compared with the previous results to verify the accuracy. The structure-properties relationships of the RHEAs are discussed over a wide temperature from 300 K to 2100 K. In addition, the effect of CSRO on the mechanical properties and deformation mechanism is analyzed.

2. Method

2.1 MD simulation

Figure 1(a)-(d) show the polycrystalline RHEA samples, which contain 20 random-crystallographic-orientation

grains built by the Voronoi construction method [26,27]. The polycrystalline RHEA sample with the size of 50 nm \times 50 nm × 50 nm has 2295393 atoms, and the lattice parameter of the BCC MoNbTaW is 3.22 Å, based on the experiment [12]. In order to comply with the Hall-Petch relationship, the average grain size of RHEA sample is 20 nm based on the previous results [26,27]. To ensure this relationship, other samples with different grain sizes are simulated (see Fig. S1). To construct the desired RHEA MoNbTaW sample with the random elements, the atoms in the polycrystal Mo are randomly replaced by atoms of Nb. Ta, and W, as presented in Fig. 1(a). This strategy is widely used to establish polycrystalline HEAs. The supercell of HEA is developed using the special quasi-random structure method, but for polycrystalline RHEA sample this is almost difficult to build. Using the large-scale MD massively parallel simulator (LAMMPS) [28], Monte Carlo (MC) and MD calculations are carried out [17,18]. The periodic boundary conditions are used for all dimensions. The RHEA sample is kept at 1800 K and then cooled to room temperature, and thus the as-cast RHEA is prepared. The annealed RHEA samples are equilibrated from the as-cast RHEA, using a hybrid MC/MD approach (Fig. 1(c) and (d)). In each MC step, a swap of one random atom with another random atom of a different type is conducted based on the Metropolis algorithm in the canonical ensemble. During every MC/MD step, 100-step MC swaps are performed followed by up to 10-step MD relaxations. Hence, the annealed polycrystalline HEAs with SRO are prepared. In addition, the degree of CSRO relies on the level of heat treatment, and then affects the deformation of HEAs. In the present work, we focus on the influence of CSRO existence on plastic behaviour and mechanical properties in the polycrystalline RHEA samples. The distribution of elements clearly reveals the short-range order of chemical elements (Fig. 1(e) and (f)). The applied temperatures are 300 K, 500 K, 800 K, and 1200 K. For each temperature, the random/annealed RHEA samples are relaxed for 100 ps by the Nose'-Hoover isobaric-isothermal (NPT) ensemble. The strain rate of 1×10⁸ s⁻¹ is applied to the random/annealed RHEA, which deforms to the tensile strain of 20% along the x direction.

The embedded atom method (EAM) potential is used to study the deformation behaviour of MoNbTaW RHEA [29,30], and is a many-body interatomic potential as follows:

$$E = F_{\alpha} \sum_{j \neq i} \rho_i \left(R_{i,j} \right) + \frac{1}{2} \sum_{j \neq i} \phi_{\alpha,\beta} \left(R_{i,j} \right), \tag{1}$$

where E is the total energy of the atomistic system, F is the sum of the embedding energy, and ϕ is the short-range pair potential energy. Here, the potential parameters of Mo, Ta, and W elements are from Zhou et al. [29], and those of Nb

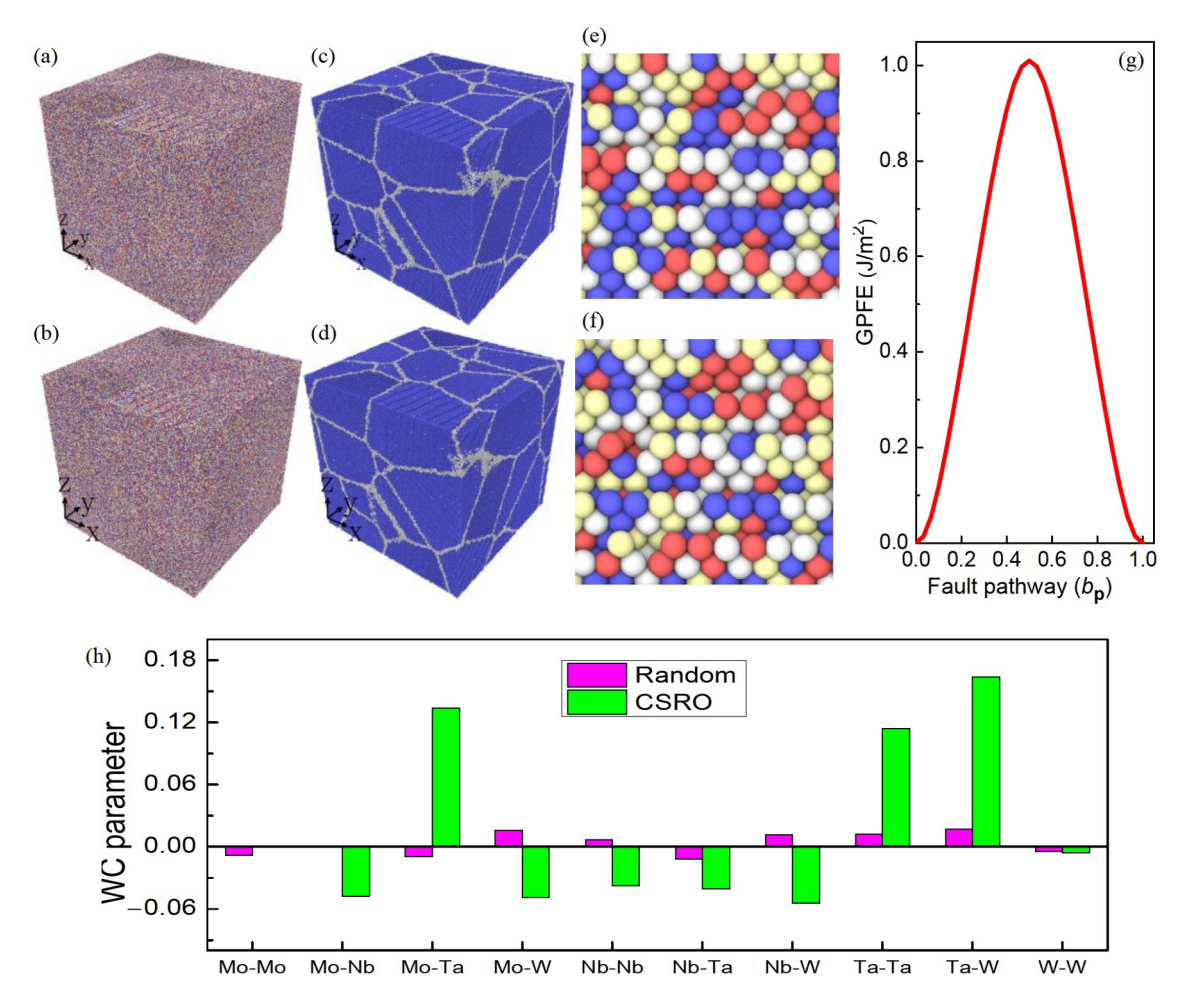


Figure 1 Atomic model for the as-cast and annealed polycrystalline HEAs. (a), (b) The atoms of the HEAs are colored based on the atomic type, where Mo, Nb, Ta, and W. (c), (d) The atoms are colored, based on the CNA value, where the BCC structure, and Other structure. (e), (f) The element distribution of the as-cast and annealed HEAs in the local area. (g) GPFE curve on (111) {110} slip system. (h) The chemical short-range order parameters of various element pairs in the as-cast and annealed RHEAs.

element are from Lin et al. [31].

The lattice parameter—cohesive energy curves in the MoNbTaW HEA using the EAM potential are presented in Fig. S1. The lattice parameter obtained from MD simulation is 3.16 Å (Fig. S1), and the corresponding error is 2% compared with experiment [12]. The elastic constants C11, C12, and C44 are 372.6, 190.2, and 100.2 GPa, which agree well with the previous result (C11 375.5, C12 167.3, and C44 101.6 GPa) [20]. Using the Voigt-Reuss-Hill approximation [32], the bulk modulus B is 251.0 GPa, in good agreement with 230.38 GPa from density functional theory [33,34], and 245 GPa from Ref. [35].

By the Ovito software [36], the evolution of the local atomic structure was distinguished via the common-neighbor analysis, where the blue color stands for the BCC structure, and the white color represents other structures, including dislocations and GB. The deformation mechanism of polycrystalline metal depends on the stable stacking fault energy, which determines the deformation twinning or dislocation glide. Hence, the curve of generalized stacking fault

energy in the RHEA is presented in Fig. 1(g). Here, the stable stacking fault energy on the {110} plane of MoNbTaW RHEA is 0.45 mJ/m² [37], and the unstable stacking fault energy on the {110} plane is 1009.9 mJ/m² in accordance with 1139 mJ/m² from the previous atomistic simulations [38], This case would lead to that the partial dislocations are more likely to occur, compared to the full dislocation.

2.2 Chemical short range order parameter

It is common to describe SRO in form of Warren-Cowley (W-C) short-range order or pair-correlation parameter, which is defined as $\alpha_{ij}^m = (p_{ij}^m - C_j)/(\delta_{ij} - C_j)$ [39], where m means the mth nearest-neighbor shell of the central atom i, p_{ij}^m is the average probability of finding a j-type atom around an i-type atom in the mth shell, C_j is the average concentration of j-type atom in the system, and δ_{ij} is the Kronecker delta function. When $\alpha_{ij}^m = 0$, this trend describes

random alloys namely in this case elements i and j are found in the alloy system. In the case of $\alpha_{ij}^m > 0$, there is a tendency of clustering or segregation of i-i and j-j pairs and for $\alpha_{ij}^m < 0$ there is a tendency of unlike pairs ordering i-j. Figure 1(h) shows that a more positive value for Ta-Ta exists, and then reveals the stronger CSRO in the annealed sample.

3 Results and discussion

To explore the effect of grain size on the mechanical properties, the grain size of polycrystalline RHEA sample is set to 15 nm, 20 nm, and 25 nm (Fig. 1 and Fig. S2). The stress-strain curves from Fig. 2(a) show the sample with small grain size exhibits higher yielding strength and flow

stress. Here, the yielding strength is defined as the 0.2% proof stress. Figure 2(b) illustrates the average flow stress (AFS) as a function of normalized grain size, indicating the Hall-Petch behavior (namely, softening with further increase of grain size). The influence of random distribution of elements in the RHEA sample with the grain size of 20 nm is explored (Figs. S3 and 3(a)). Figure 3(a) plots the stressstrain curves for the five independent samples with the random element distributions. The ultimate tensile strength (UTS), which is the maximum stress value from the stressstrain curve, 7.5±0.07 GPa, and AFS is 6.4±0.2 GPa from Fig. 3(a). Thus, the random element distribution has a weak influence on mechanical properties. Hence, the results of the current random element distribution can represent the general laws of the MoNbTaW RHEA. In addition, the role of strain rate is also considered in the as-cast RHEA sample with the grain size of 20 nm (Fig. 3(b)), and the obvious

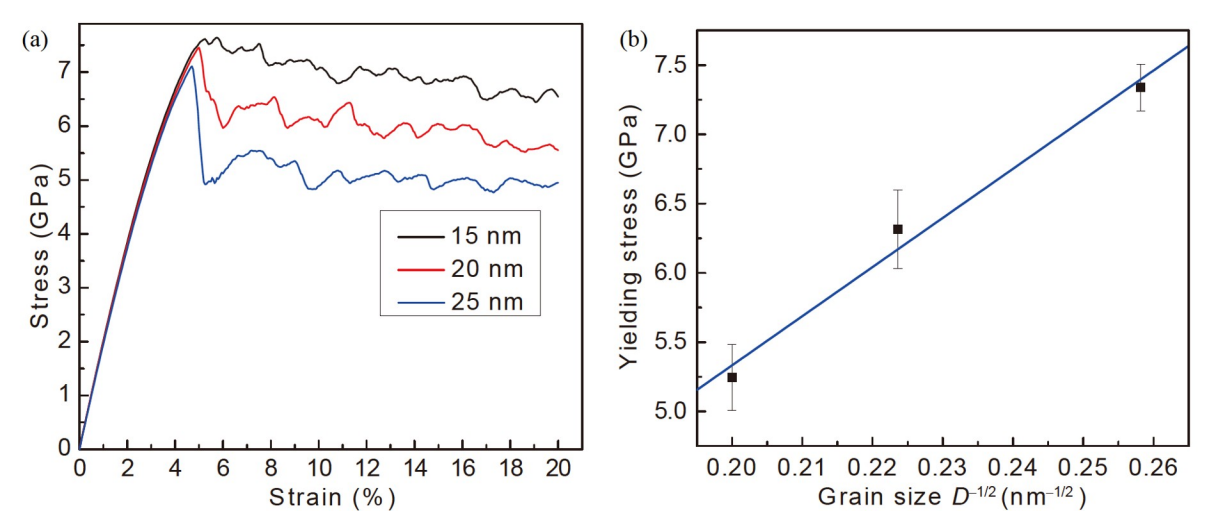


Figure 2 (a) Stress-strain curve of the as-cast RHEA with different grain sizes. (b) AFS as a function of (grain size)^{-1/2} for the as-cast RHEA.

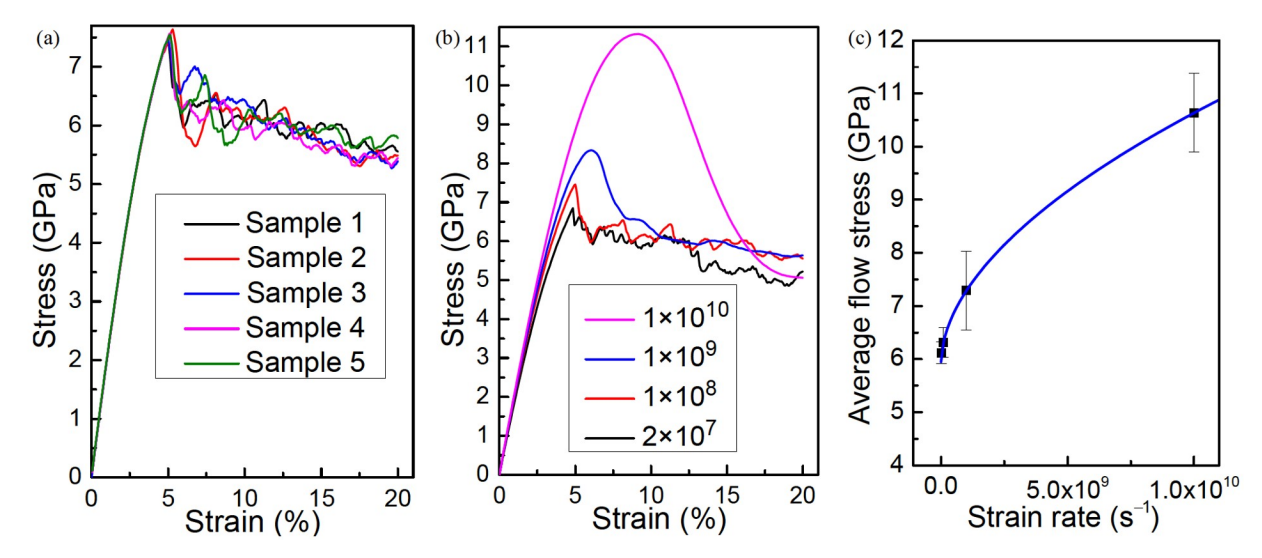


Figure 3 (a) Stress-strain curve of the as-cast RHEA with different element distributions for the grain size of 20 nm. (b) Stress-strain curve of the as-cast RHEA with the grain size of 20 nm under different strain rates. (c) Relationship of the AFS and strain rate, and the corresponding fitting curve.

strain rate dependent mechanical properties are observed. Figure 3(c) shows the relation between the mechanical property and strain rate, and the corresponding fitting curve using a power function relationship of $\sigma_y = a + b\dot{\varepsilon}^c$ ($\sigma_y = 5.947 + 1.694^{-5}\dot{\varepsilon}^{0.5442}$). Based on the power function relationship, the value of the flow stress at a quasistatic state ($\dot{\varepsilon} \rightarrow 0$) is 5.947 GPa, in good agreement with 5.3 GPa based on the polycrystalline MoNbTaW RHEAs with grain size of 10 nm [40].

To study the effect of temperature on the mechanical response, the as-cast, and annealed RHEAs are placed at the temperatures of 300, 800, 1200, 1500, 1800, and 2100 K, and then tensile deformed. Figure 4(a) and (b) shows the representative tensile engineering stress-strain curves of the polycrystalline RHEA samples. In general, the tensile deformation of polycrystalline samples presents the initial elastic deformation, the yield deformation along with the large and abrupt stress drop, and the stable plastic deformation at the low stress [27,30]. This typical stress-strain relationship also occurs in the single crystal and polycrystalline traditional metal materials [41]. The flow stress fluctuates sharply in a zigzag pattern with the increasing strain attributed to the frequent dislocation behaviors (dislocation nucleation, dislocation emission, and dislocation motion), which are observed in the previous work [27,41]. In addition, the bulk RHEA at the high temperature of 2100 K exhibits the excellent yield strength. After the strain hardening, the flow stress shows the jagged sharp fluctuations with the strain (Fig. 4(a) and (b)). The increasing temperature reduces the strain hardening rate and the amplitude of fluctuations in the flow stress [27]. The phenomenon has also been experimentally verified, where strainhardening rate decreases at high temperature in the polycrystalline copper [42]. In the annealed RHEAs, UTS and AFS decrease because the formation of ordered structures reduces other element solute concentration within the matrix for the annealed structure (Fig. 4(c)). Thus, the solid solution strengthening reduces, resulting in low UTS and AFS. The annealed structure increases the average error value of AFS, thus reducing the stability of mechanical properties due to the existence of the CSRO structure.

To deeply understand the origin of the complex dynamic mechanical properties, the evolution of microstructure with the increased strain and temperature should be investigated in detail. Figure \$4 shows the grain evolution and grainboundary movement at various temperatures. The increased temperature would cause grain-boundary thickening along with the initiation of grain boundary migration [27], and the degradation of mechanical properties seems inevitable during the plastic deformation (Fig. 4(c)). A large number of the fine amorphous phases are nucleated, and thus, a structural instability of the high-temperature RHEA takes place [43,44]. The high strain also leads to the increased structural instability (Fig. S4). It can be noted that the crystal-to-amorphous phase transition takes place under the loading in HfNbTaZr RHEA and at high stress in the ultrafine-grained HEA CrMnFeCoNi [45,46]. In addition, the annealed structure would result in the obvious microstructural evolution [47], such as grain boundary characteristics, and deformation twinning (Fig. 5). In the HEAs with hard-intermetallic compounds, deformation twinning can lead to an excellent combination of strength, ductility, and strain-hardening ability [47]. Here, the heterogeneous nucleation of deformation twinning with the increased strain is observed in the as-cast and annealed RHEA. The growth of deformation twinning is mediated by partial dislocation activities at the twin boundary. In particular, the distribution

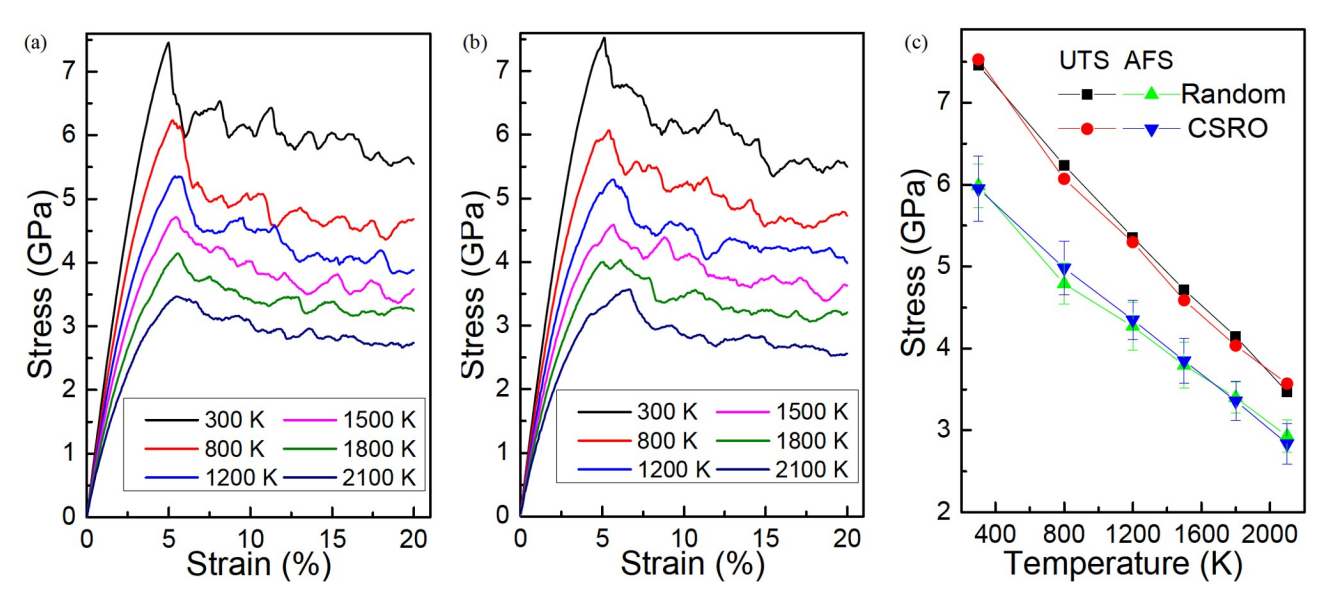


Figure 4 Stress-strain curve of the (a) as-cast and (b) annealed RHEA. (c) UTS and AFS from the strain range of 6%-20% with the increased temperature.

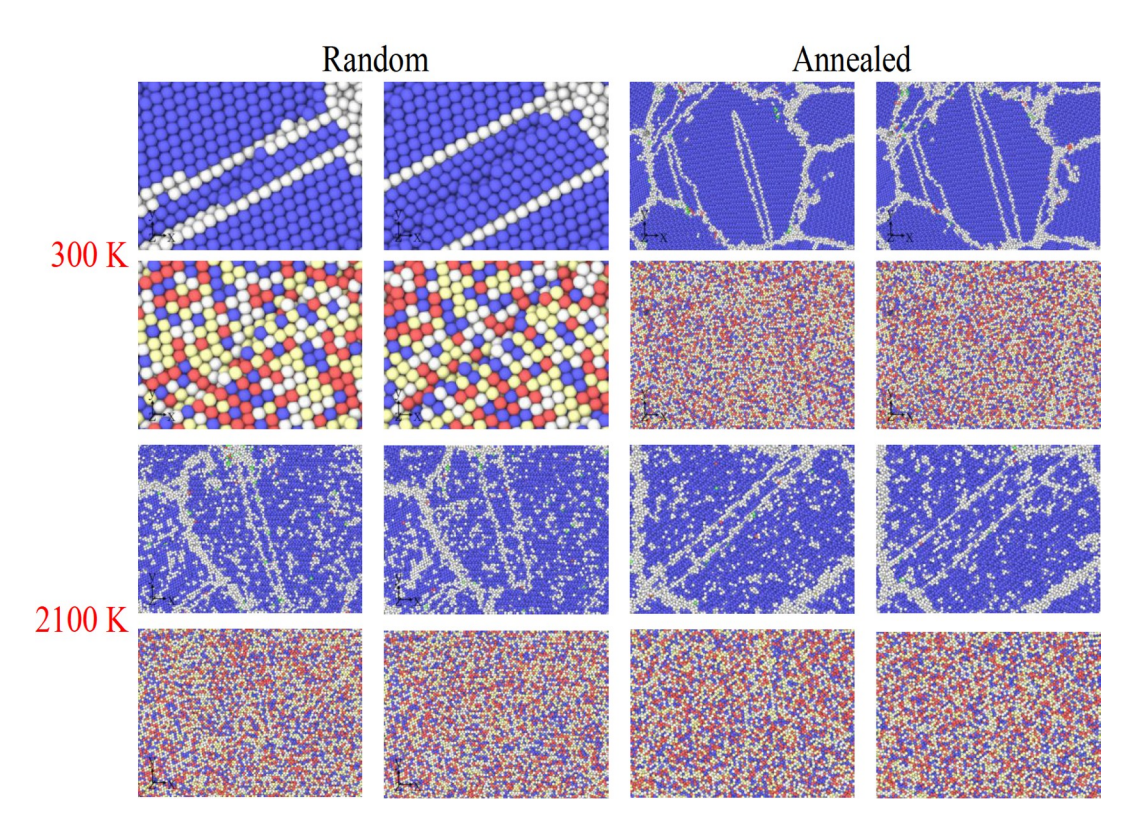


Figure 5 Deformation twinning of as-cast and annealed RHEA at the temperature of 300 K and 2100 K.

of chemical elements also shows that the plastic deformation causes the elemental redistribution (Fig. 5). Hence, the deformation twinning plays a key role in the deformation mechanism. The local deformation is further accommodated via the dislocation-based plasticity, and amorphous nucleation in the grains.

To clearly observe the degree of plastic deformation, the shear strain distribution should be quantified in the deformed RHEA. Figure S5 shows the shear strain distribution with the increase of strain and temperature. Here, each atom is colored according to the local von Mises shear invariant in the initially stable atomic configurations during the defamation [27,30]. For various temperatures, the high strain region in the as-cast and annealed RHEA occurs along the grain boundary. With the continuous plastic deformation, the strain at the grain boundary continues to increase and the region of microstructure evolution in grains also produces an obvious high strain (Figs. S5 and S6). The high temperature causes the strain diffuses along the grain boundary to both sides [48,49], due to the observed grain boundary thickening during loading. However, the stress distribution is not completely consistent with the strain distribution (Figs. S5 and S6). The low stress takes place near the grain boundary, and the high stress exists within the grains (Fig. S6). The high temperature causes the decrease of the amplitude of the stress, resulting in a high temperature softening effect due to the weak atomic bonds (Fig. S6). The detailed comparisons of Figs. S5 and S6 show that the CSRO affects the stress and strain partition dependent upon the mechanical properties (Fig. 4). The short-range ordering as hetero-structure causes that the strong incompatibility induced a large strain gradient in Al-Mg-Sc alloy [50].

The dislocation structures play an important role in determining both the deformation mechanism and material properties [51-54]. Here, the distributions of dislocation activities among HEAs are presented in Figs. S7 and S9, where the lines are colored based on the Burgers vector and geometric configuration. The 1/2(111) and other dislocations account for a large proportion of the forest dislocations [54-56]. The increased temperature would obviously reduce the dislocations, and the other dislocations would drop sharply (Fig. S7). Compared with the traditional alloys, a large number of the edge-type dislocations occur after the deformation. This trend is different from the classic view of the screw-dislocation-controlled material deformation [57]. Additionally, it can be seen that the CSRO structure plays a significant role in determining the dislocation hardening behavior (Fig. S8). The presence of SRO significantly affects the dislocation motion, due to the low solute drag effect [18]. Meanwhile, the CSRO structure would provide some pinning points in the space range to reduce the mean free paths, owing to the interactions of the slip dislocations with the forest dislocations and their subsequent storage.

To quantitatively evaluate the effects of the strain and dislocation density on the mechanical properties, their statistical results are presented in Fig. 6. The strain shows the

sharp fluctuations along the tensile direction in the as-cast and annealed RHEAs, and then controls the nucleation and slip resistance of dislocations (Fig. 6(a) and (b)). These massive dislocation behaviors would determine the strength and toughness of RHEA. Figure 6(a) and (b) also show that the distribution of the shear strain in the deformed RHEA is significantly inhomogeneous. The value of the maximum shear strain depends upon the variations of the location and given temperature. The statistical value for dislocation density is plotted in Fig. 6(c). The decreased dislocation density with the increase of temperature further verifies this viewpoint for the relationship of the CSRO structure and microstructural variables (Fig. 6(c)). The large degree of the CSRO modeled as obstacles would effectively inhibit the dislocation nucleation and motion, and fundamentally improves the mechanical properties.

4. Theoretical modeling

4.1 Yield strength of as-cast and annealed HEAs

Based on the previous work [58-60], a microstructure-based and mechanism-based constitutive model is proposed to investigate the mechanical behaviors of the as-cast and annealed RHEAs. The establishment of constitutive relation refers to the previous works [27,55], the flow stress of RHEAs is expressed as

$$\sigma_{\text{Flow}} = \sigma_{\text{Solid}} + \sigma_{\text{Grain}} + \sigma_{\text{Dislocation}} + \sigma_{\text{Twin}} + \sigma_{\text{Back}} + \sigma_{\text{CSRO}},$$
 (2)

where $\sigma_{\rm Solid}$ is the solid solution strengthening which is caused by severe lattice distortion, $\sigma_{\rm Grain}$ is the grain-boundary strengthening, $\sigma_{\rm Dislocation}$ is the dislocation strengthening, $\sigma_{\rm Twin}$ is the twinning strengthening, $\sigma_{\rm Back}$ is the back stress, and $\sigma_{\rm CSRO}$ is the contribution of the CSRO to

strengthening. The strength contribution of the linear combination mechanisms has been widely adopted in evaluating the performance of HEAs [27,55,58]. The constitutive model used in this work is independent of the strain rate [61,62].

The expression of the lattice-distortion-dependent solidsolution strengthening introduced by a single element in RHEAs is expressed as [58]

$$\sigma_{\text{Solid}} = \sum_{i}^{n} AGc_{i}^{5/3} \delta p_{i}^{4/3}, \qquad (3)$$

where A is a material-dependent constant, n is the total number of elements, G is the shear modulus, c_i is the atomic concentration of the element i, and δp_i is the mismatch parameter of element i.

The mismatch parameter consists of the shear modulus mismatch $\delta G_{i,ijkl}$ and atomic radius mismatch $\delta r_{i,ijkl}$. δp_i , $\delta G_{i,ijkl}$, and $\delta r_{i,ijkl}$ are expressed as

$$\delta p_i = \xi \left(\delta G_{i,ijkl}^2 + \beta^2 \delta r_{i,ijkl}^2 \right)^{1/2},\tag{4}$$

$$\delta G_{i,ijkl} = \frac{\delta G_{ijkl}^{\text{Ave}} - \delta G_{jkl}^{\text{Ave}}}{c_i},\tag{5}$$

$$\delta r_{i,ijkl} = \frac{\delta r_{ijkl}^{\text{Ave}} - \delta r_{jkl}^{\text{Ave}}}{c_i},\tag{6}$$

where $\xi=2.5$ in the BCC metals, the value of β depends on the dislocation type, and $\beta=3$ in the BCC HEAs as the main dislocation type is the screw dislocation. $\delta G_{ijkl}^{\text{Ave}}$ and $\delta r_{ijkl}^{\text{Ave}}$ are the average modulus mismatch and average atomic radius mismatch of the ijkl alloy, respectively. The average modulus mismatch and average atomic radius mismatch are expressed as

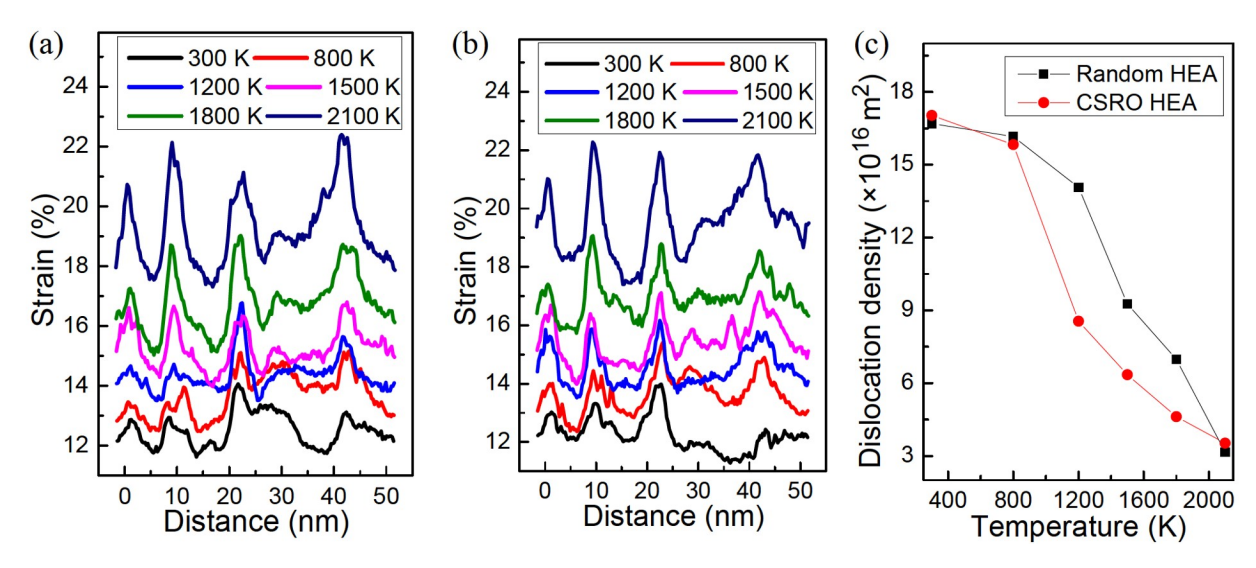


Figure 6 Strain evolution along the tensile direction at the strain of 10% in the (a) as-cast and (b) annealed RHEAs. (c) The dislocation density with the increased temperature at the strain of 10%.

$$\delta G^{\text{Ave}} = \sum_{i}^{n} \sum_{j}^{n} c_{i} c_{j} \delta G_{ij}$$

$$= (c_{1} \quad c_{2} \quad \cdots \quad c_{n}) \begin{pmatrix} \delta G_{11} & \delta G_{12} & \cdots & \delta G_{1n} \\ \delta G_{21} & \delta G_{22} & \cdots & \delta G_{2n} \\ \vdots & \cdots & \ddots & \vdots \\ \delta G_{n1} & \delta G_{n2} & \cdots & \delta G_{nn} \end{pmatrix} \begin{pmatrix} c_{1} \\ c_{2} \\ \vdots \\ c_{n} \end{pmatrix},$$

$$(7)$$

$$\delta r^{\text{Ave}} = \sum_{i}^{n} \sum_{j}^{n} c_{i} c_{j} \delta r_{ij}$$

$$= \begin{pmatrix} c_{1} & c_{2} & \cdots & c_{n} \end{pmatrix} \begin{pmatrix} \delta r_{11} & \delta r_{12} & \cdots & \delta r_{1n} \\ \delta r_{21} & \delta r_{22} & \cdots & \delta r_{2n} \\ \vdots & \cdots & \ddots & \vdots \\ \delta r_{1} & \delta r_{2} & \cdots & \delta r_{n} \end{pmatrix} \begin{pmatrix} c_{1} \\ c_{2} \\ \vdots \\ c_{n} \end{pmatrix}, \quad (8)$$

where δG_{ij} and δr_{ij} are the shear modulus mismatch and atomic radius mismatch between element i and j, respectively, and they are expressed by

$$\delta G_{ij} = 2(G_i - G_j)/(G_i + G_j), \tag{9}$$

$$\delta r_{ii} = 2(r_i - r_i)/(r_i + r_i),$$
 (10)

where G_i is the shear modulus, and r_i is the atomic radius of element i.

According to the Hall-Petch relationship, the grain-size strengthening contributed to the flow stress is expressed as [63]

$$\sigma_{\text{Grain}} = k_{\text{HP}} / \sqrt{d}$$
, (11)

where $k_{\rm HP}$ is the Hall-Petch coefficient, and the estimated value is 590 MPa·um^{1/2} which is reported for NbMo-TaWVCr HEA [64], and d is the grain size. The Hall-Petch coefficient reflects the overall influence of grain boundary on dislocation, including the strengthening effect due to grain boundary hindering dislocation and the softening effect due to grain boundary emitting dislocations. Logically, the CSRO will enhance the dislocation emission from grain boundaries, thereby decreasing the Hall-Petch coefficient. However, the Hall-Petch coefficient used in this work is obtained from experiments, which already consider the influence of CSRO in default. In this case, the effect of CSRO on grain boundary strengthening is not considered in this model. Based on the research of Wagner and Laplanche [65], the Hall-Petch slope is related to the critical strength of grain or twin boundaries against slip transmission. Due to the lack of a theoretical formula for the relationship between the Hall-Petch slope and stacking fault energy or temperature for RHEA, the effect of stacking fault energy and temperature on grain boundary strengthening is not considered in this work.

Based on the Bailey-Hirsch relationship, the dislocation strengthening contributed to the flow stress is calculated as [66]

$$\sigma_{\text{Dislocation}} = M\alpha G b \sqrt{\rho},$$
 (12)

where M is the Taylor factor, α is the empirical constant, b is the burgers vector, and ρ is the dislocation density.

Based on the Kocks-Mecking model [67], the dislocation density is estimated by

$$\frac{\partial \rho}{\partial \varepsilon_{p}} = M \left[\frac{1}{bd} + \frac{\psi \sqrt{\rho}}{b} - k_{20} \left(\frac{\varepsilon_{p}'}{\varepsilon_{0}'} \right)^{-m_{1}} \rho \right], \tag{13}$$

where ε_p is the plastic strain, ψ is the proportionality factor, k_{20} is the dynamic recovery constant, ε_p' is the plastic strain rate, ε_0' is the reference strain rate, and m_1 is the dynamic recovery constant. Equation (13) describes the multiplication and annihilation of dislocations, dislocation evolution is completely dependent on plastic strain and material microstructure parameters. The model does not involve the nucleation stress of dislocations.

The critical twin thickness decides the deformation twinning strengthening, and the deformation twins are expressed as [68]

$$\sigma_{\text{Twin}} = \begin{cases} M \left[\chi G \frac{\pi (2 - v) \lambda e_{\text{T}}}{8 d (1 - v)} + \frac{\varphi \gamma_{\text{tb}}}{\lambda e^{\text{T}}} \right] f, & \lambda \leq \lambda_{\text{c}}, \\ M \frac{1}{p_{\text{g}}} \left(\frac{\gamma_{\text{sf}}}{b} + \frac{G b_{\text{p}}}{3 \lambda} \right) f, & \lambda \leq \lambda_{\text{c}}, \end{cases}$$
(14)

where χ is the unit order coefficient, v is the Poisson ratio, λ is the twin thickness, $e_{\rm T}$ is the shear strain for transformation, φ is the twin boundary forming process-dependent coefficient, γ_{tb} is the stacking fault energy of the twin, f is the twin volume fraction, p_g is the geometrical parameter, $\gamma_{\rm sf}$ is the stacking fault energy, and $b_{\rm p}$ is the Burgers vector of a partial dislocation. Here, when the twin boundary is completely detwinned, $\varphi = -2$; when the twin boundary is formed, $\varphi = 2$; and when the twin boundary is thickening or thinning, $\varphi = 0$. The MD simulations show that the twin boundary is thickening continuously during the deformation stage (Fig. S4). Thus, φ is equal to 0 in Eq. (14). This model focuses on the twinning strengthening contribution to the yield strength. The deformation twinning occurs during the plastic deformation process, which is computed based on the previous work [18].

The back stress is originating from the accumulation of dislocations at grain boundaries [69], it is expressed as

$$\sigma_{\text{Back}} = M \frac{Gb}{d} N, \tag{15}$$

where N is the number of dislocations accumulating at grain boundaries, which can be determined by the plastic-strain evolution law, as shown in the following:

$$\frac{\mathrm{d}N}{\mathrm{d}\varepsilon_{\mathrm{p}}} = \frac{\varsigma}{b} \left(1 - \frac{N}{N_{\mathrm{B}}} \right),\tag{16}$$

where ς is the mean distance between slip bands, and $N_{\rm B}$ is

the maximum number of pileup dislocations at the grain boundaries.

Based on the previous work [27], non-uniform deformation exists in MD simulation. The geometrically necessary dislocations would be generated to accommodate the non-uniform deformation near the grain boundary [70]. The back stress is a long-range internal stress caused by the interaction and pile-up of geometrically necessary dislocations near the grain boundaries. The Hall-Petch expression is used to describe the hindering effect of the grain boundaries themselves on dislocations. Thus, there are two independent mechanisms considered in this model.

According to the previous work [71], the contribution of the CSRO to strengthening in BCC alloys is calculated as follows:

$$\sigma_{\rm CSRO} = M \left(\frac{3.264}{L_{\rm p}^3} \right) \sum_{i} \left(\sum_{j} c_i c_j \alpha_{ij}^m U_{ij} \right), \tag{17}$$

where L_p is the lattice parameter of the BCC unit cell, U_{ij} is the pair interaction energy between elements i and j at first and second neighbors [72,73].

The corresponding parameters used at room temperature and strain rate of $1 \times 10^8 \, \mathrm{s}^{-1}$ are listed in Table 1. Because these parameters depend on the temperature and strain rate, only the case of room temperature and given strain rate is taken as an example. If one wants to obtain the flow stress of RHEA at different strain rates and temperatures, the corresponding microstructure parameters, such as grain size, twin thickness, stacking fault energy, and twinning energy rely on the MD simulation results, which should be defined as the

Table 1 Parameters used in this model for the MoNbTaW RHEA at room temperature and the strain rate of $1\times10^8~{\rm s}^{-1}$

| Parameter | Symbol | Magnitude |
|--|-------------------|------------|
| Material-dependent constant | A | 0.05 |
| Grain size (nm) | d | 20 |
| Taylor factor | M | 2.733 [74] |
| Empirical constant | α | 0.2 |
| Burgers vector (nm) | b | 0.278 [75] |
| Proportionality factor | Ψ | 0.025 [27] |
| Dynamic recovery constant | k_{20} | 13.4 [27] |
| Reference strain rate | $arepsilon_0^{'}$ | 1 [27] |
| Dynamic recovery constant | m_1 | 21.25 [27] |
| Unit order coefficient | χ | 0.4 [27] |
| Poisson ratio | v | 0.3 |
| Twin thickness (nm) | λ | 1.2 |
| Shear strain for transformation | e_{T} | 0.707 [27] |
| Stacking fault energy of twin (mJ/m²) | γ_{tb} | 0.45 |
| Geometrical parameter | $p_{ m g}$ | 1.8 [27] |
| Stacking fault energy (mJ/m²) | $\gamma_{ m sf}$ | 0.45 |
| Burgers vector of partial dislocation (nm) | b_{p} | 0.25 |
| Mean spacing between slip bands (nm) | ς | 1 [27] |
| Maximum number of dislocation loops | $N_{ m B}$ | 10 [27] |
| lattice parameter (Å) | L_{p} | 3.22 |

functions of the room temperature and the strain rate. To predict the high-temperature performance of RHEAs, in addition to the microstructure evolution provided by the MD simulation, the numerical values of these constitutive parameters at high temperatures are required, which are challenging.

To uncouple the influence of various microstructures on the mechanical properties, the separate contribution of different strengthening mechanisms on the flow stress of the as-cast and annealed MoNbTaW RHEAs under the condition of room temperature and strain rate of 1×10^8 s⁻¹ are calculated, as shown in Fig. 7. To verify the accuracy of the theoretical model for yield strength in the MoNbTaW RHEAs, the prediction results are compared with the MD simulation results. The yield strength from where a specified offset at 0.2% strain parallel to the slope intercepts the stress-strain curve, and the yield strength values of the ascast and annealed MoNbTaW RHEAs obtained by MD simulation are 5.25 GPa and 5.4 GPa (Fig. 4(a) and (b)). Figure 7(a) and (c) show the yield strength values for the ascast and annealed MoNbTaW RHEAs calculated by the theoretical model are 5.29 GPa and 5.47 GPa. The errors for the as-cast and annealed RHEAs are 0.76% and 1.30%, respectively. These findings demonstrate that the theoretical model is highly accurate.

It can be seen from Fig. 7 that the flow stress is dominated by the solid solution strengthening and grain boundary strengthening, in consistent with previous experiments [12,16]. Due to the nanometer grain size, the current calculation results in Fig. 7 do not show significant strain hardening, which is consistent with the results of MD simulation and experimental results [70,76]. The contribution of the grain-size strengthening to the yield stress is greater than that of solid solution strengthening (Fig. 7(b)). In addition, the strain hardening stems from the back stress (Fig. 7(a)), because the post-yield flow stress keeps increasing after the back stress is added. Surprisingly, the contributions of dislocation strengthening and twinning strengthening on both the flow stress (Fig. 7(a)) and strain hardening (Fig. 7(b)) are small.

Figure 7(c) and (d) show the effects of different strengthening mechanisms on the flow stress at room temperature in the annealed MoNbTaW RHEA. Note that the annealing process triggers the formation of CSRO, which causes extra strengthening compared with the as-cast sample. As can be seen from Fig. 7(c), CSRO strengthening slightly enhanced the flow stress, and $\sigma_{\rm CSRO}$ = 180 MPa (Fig. 7(d)). However, compared with the contribution of other strengthening mechanisms, such as solid solution strengthening and grain-size strengthening, the contribution of CSRO is small (Fig. 7(d)), which is basically consistent with the results of MD simulation [73]. The theoretically predicted result echoes the results of MD simulation, where

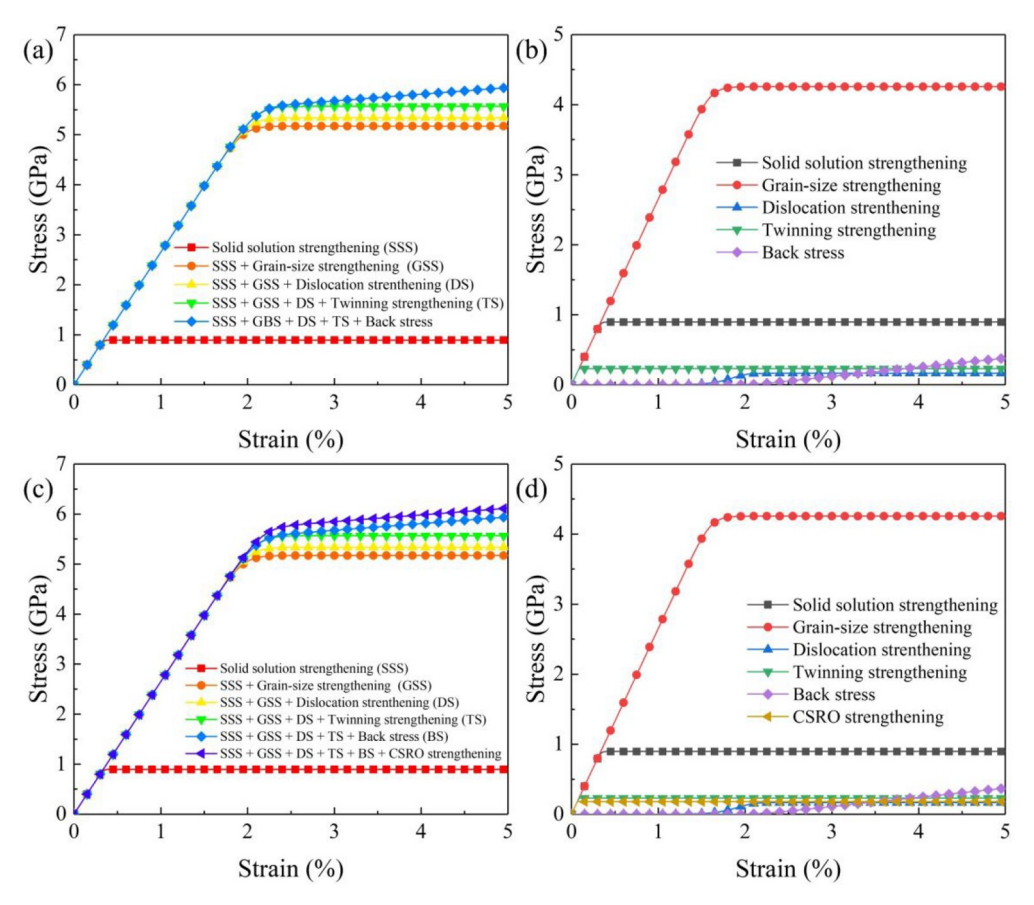


Figure 7 Stress-strain curves of the as-cast and annealed MoNbTaW RHEAs under the uniaxial tensile deformation. (a) The flow stresses of the as-cast MoNbTaW RHEA after the superposition of different strengthening mechanisms. (b) The separate contribution of different strengthening mechanisms on the flow stress in the as-cast MoNbTaW RHEA. (c) The flow stresses of the annealed MoNbTaW RHEA after the superposition of different strengthening mechanisms. (d) The separate contribution of different strengthening mechanisms on the flow stress in the annealed MoNbTaW RHEA.

the yield strength of MoNbTaW RHEA is only increased by 150 MPa after annealing. Here, it is worth noting that the formation of CSRO would change the element distribution in the material, thus affecting the solid solution degree. Therefore, the minor effect of CSRO predicted in this work implies the competition between CSRO strengthening and solid solution strengthening in RHEAs.

4.2 Difference of lattice distortion between annealed and as-cast HEAs

Based on the work [77], the interatomic spacing of a solid solution can be regarded as the average spacing of all atoms in the selected lattice region, it also can be applied to the annealed HEA with CSRO. Hence, the averaging atomic size mismatch $\delta r_{\rm CSRO}^{\rm Ave}$ and averaging elastic mismatch $\delta G_{\rm CSRO}^{\rm Ave}$ in the annealed HEA can be stated as follows:

$$\delta r_{\rm CSRO}^{\rm Ave} = \sum_{i}^{n} \sum_{j}^{n} \delta r_{ij} \cdot p_{ij}, \qquad (18)$$

$$\delta G_{\text{CSRO}}^{\text{Ave}} = \sum_{i}^{n} \sum_{j}^{n} \delta G_{ij} \cdot p_{ij}, \qquad (19)$$

where p_{ij} is the average probability of finding a *j*-type atom around an *i*-type atom in the 1st shell.

Due to the calculation needs, the ijkl HEA is divided into two parts. They are the additional element i and matrix jkl. The change in the atomic percentage of element i, c_i , would lead to the change in the atomic-size mismatch $\delta r_{i,ijkl}^{\rm CSRO}$ and the elastic mismatch $\delta G_{i,ijkl}^{\rm CSRO}$. The two mismatches in annealed HEA with CSRO can be expressed as

$$\delta r_{i,ijkl}^{\text{CSRO}} = \frac{\delta r_{\text{CSRO},ijkl}^{\text{Ave}} - \delta r_{\text{CSRO},jkl}^{\text{Ave}}}{c_i},$$
(20)

$$\delta G_{i,ijkl}^{\text{CSRO}} = \frac{\delta G_{\text{CSRO},ijkl}^{\text{Ave}} - \delta G_{\text{CSRO},jkl}^{\text{Ave}}}{c_i},$$
(21)

where $\delta r_{\text{CSRO},ijkl}^{\text{Ave}}$ and $\delta r_{\text{CSRO},jkl}^{\text{Ave}}$ can be obtained through Eq. (18), $\delta G_{\text{CSRO},ijkl}^{\text{Ave}}$ and $\delta G_{\text{CSRO},jkl}^{\text{Ave}}$ are calculated by Eq. (19).

Based on Eqs. (5)-(6) and Eqs. (20)-(21), the differences of the atomic-size mismatch and the elastic mismatch between the annealed and as-cast HEAs are presented in Fig. 8. The atomic-size mismatch and elastic mismatch in annealed HEA with CSRO are larger than that of as-cast

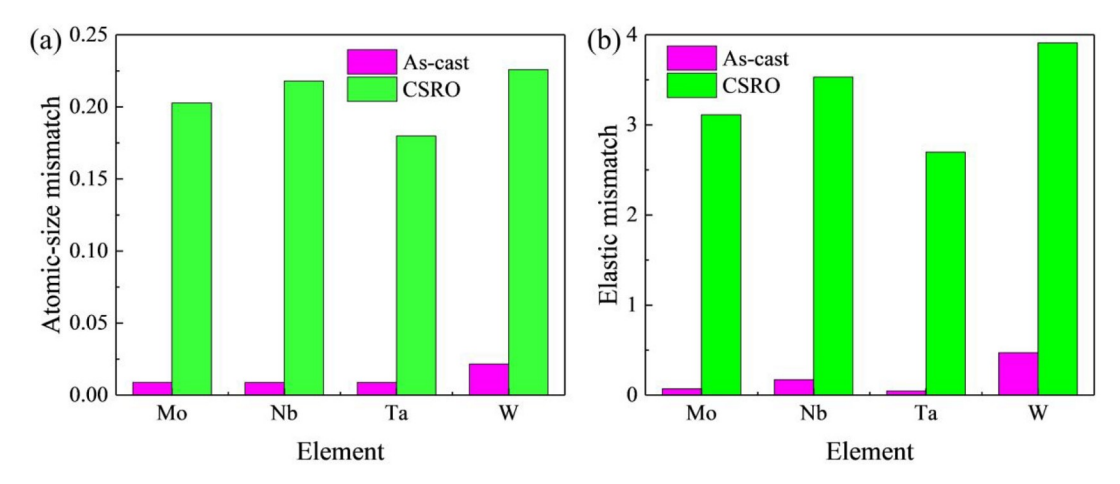


Figure 8 Difference of the (a) atomic-size mismatch and (b) the elastic mismatch between the annealed and as-cast HEAs.

HEA. A recent study shows the differences of chemical affinities in MoTaTiWZr RHEA are the driving force for the CSRO, which could enhance the energy barriers for the dislocation motion [78]. This key role would influence strongly the mechanical properties, and the model for the corresponding strength contribution should be developed in the future.

5. Conclusion

In the present work, the deformation mechanisms of the equiatomic MoNbTaW RHEAs under the uniaxial tension are investigated using the MD simulation methods, and the influences of chemistry and temperature on the mechanical response are studied. A microstructure-based constitutive model is established to estimate the effects of the multiple strengthening mechanisms. After the strain hardening, the flow stress presents the jagged sharp fluctuations with the increased strain. The high temperature causes the reduction of the strain hardening rate and the fluctuation amplitude of the flow stress, due to the low solute concentrations in the annealed structure. The stress and strain partition depends upon the mechanical properties. In the condition of room temperature and the strain rate of 1×10⁸ s⁻¹, the solid solution strengthening and grain boundary strengthening contribute considerably to the flow stress, and twinning strengthening contributes little to the flow stress compare with the solid solution strengthening and grain boundary strengthening. The strengthening contribution from CSRO is limited compared with traditional strengthening mechanism. Moreover, as a theoretical guideline and instruction, our work contributes to atomic-scale insight into the deformation behavior and strain hardening of RHEAs.

Conflict of interest On behalf of all authors, the corresponding author states that there is no conflict of interest.

Author contributions Jia Li: Conceptualization, Methodology, Writing – original draft, Writing – review & editing, Formal analysis, Software, Investigation, Data curation, Validation, Supervision, Funding acquisition. Siwei Ren: Formal analysis, Software, Writing – original draft, Writing – review & editing, Investigation, Data curation. Bin Liu: Conceptualization, Validation, Supervision. PK Liaw: Writing – review & editing, Project administration, Supervision, Funding acquisition. Qihong Fang: Conceptualization, Methodology, Validation, Writing – review & editing, Supervision, Funding acquisition.

Acknowledgements This work was supported by the National Natural Science Foundation of China (Grant Nos. U2267252, 12172123, and 12072109), the Natural Science Foundation of Hunan Province (Grant Nos. 2022JJ20001 and 2021JJ40032), the Science and Technology Innovation Program of Hunan Province (Grant No. 2022RC1200), the National Science Foundation (Grant Nos. DMR-1611180, 1809640, and 2226508), and the Army Research Office (Grant Nos. W911NF-13–1-0438 and W911NF-19–2-0049).

- T. M. Smith, B. D. Esser, N. Antolin, A. Carlsson, R. E. A. Williams, A. Wessman, T. Hanlon, H. L. Fraser, W. Windl, D. W. McComb, and M. J. Mills, Phase transformation strengthening of hightemperature superalloys, Nat. Commun. 7, 13434 (2016).
- G. Chen, Y. Peng, G. Zheng, Z. Qi, M. Wang, H. Yu, C. Dong, and C. T. Liu, Polysynthetic twinned TiAl single crystals for hightemperature applications, Nat. Mater 15, 876 (2016).
- 3 A. Manzoni, S. Singh, H. Daoud, R. Popp, R. Völkl, U. Glatzel, and N. Wanderka, On the path to optimizing the Al-Co-Cr-Cu-Fe-Ni-Ti high entropy alloy family for high temperature applications, Entropy 18, 104 (2016).
- 4 O. N. Senkov, G. B. Wilks, J. M. Scott, and D. B. Miracle, Mechanical properties of Nb25Mo25Ta25W25 and V20Nb20Mo20-Ta20W20 refractory high entropy alloys, Intermetallics 19, 698 (2011)
- O. N. Senkov, S. Gorsse, and D. B. Miracle, High temperature strength of refractory complex concentrated alloys, Acta Mater. 175, 394 (2019).
- O. N. Senkov, D. B. Miracle, K. J. Chaput, and J. P. Couzinie, Development and exploration of refractory high entropy alloys—A review, J. Mater. Res. 33, 3092 (2018).
- 7 D. Luo, Q. Zhou, W. Ye, Y. Ren, C. Greiner, Y. He, and H. Wang, Design and characterization of self-lubricating refractory high entropy alloy-based multilayered films, ACS Appl. Mater. Interfaces 13, 55712 (2021).
- 8 R. Feng, B. Feng, M. C. Gao, C. Zhang, J. C. Neuefeind, J. D. Poplawsky, Y. Ren, K. An, M. Widom, and P. K. Liaw, Superior high-temperature strength in a supersaturated refractory high-entropy

- alloy, Adv. Mater. 33, 2102401 (2021).
- 9 Z. Wang, H. Wu, Y. Wu, H. Huang, X. Zhu, Y. Zhang, H. Zhu, X. Yuan, Q. Chen, S. Wang, X. Liu, H. Wang, S. Jiang, M. J. Kim, and Z. Lu, Solving oxygen embrittlement of refractory high-entropy alloy via grain boundary engineering. Mater. Today 54, 83 (2022).
- 10 B. Xiao, W. Jia, H. Tang, J. Wang, and L. Zhou, Microstructure and mechanical properties of WMoTaNbTi refractory high-entropy alloys fabricated by selective electron beam melting, J. Mater. Sci. Tech. 108, 54 (2022).
- 11 X. J. Fan, R. T. Qu, and Z. F. Zhang, Remarkably high fracture toughness of HfNbTaTiZr refractory high-entropy alloy, J. Mater. Sci. Tech. 123, 70 (2022).
- 12 A. Kanchi, K. V. Rajulapati, B. S. Rao, D. Sivaprahasam, and R. C. Gundakaram, Influence of thermomechanical processing on microstructure and mechanical properties of MoNbTaW Refractory high-entropy alloy, J. Mater. Eng. Perform. 31, 7964 (2022).
- M. A. Melia, S. R. Whetten, R. Puckett, M. Jones, M. J. Heiden, N. Argibay, and A. B. Kustas, High-throughput additive manufacturing and characterization of refractory high entropy alloys, Appl. Mater. Today 19, 100560 (2020).
- 14 M. Moorehead, K. Bertsch, M. Niezgoda, C. Parkin, M. Elbakhshwan, K. Sridharan, C. Zhang, D. Thoma, and A. Couet, Highthroughput synthesis of Mo-Nb-Ta-W high-entropy alloys via additive manufacturing, Mater. Des. 187, 108358 (2020).
- 15 Y. Zong, N. Hashimoto, and H. Oka, Study on irradiation effects of refractory bcc high-entropy alloy, Nucl. Mater. Energy 31, 101158 (2022).
- 16 D. G. Kalali, S. Antharam, M. Hasan, P. S. Karthik, P. S. Phani, K. Bhanu Sankara Rao, and K. V. Rajulapati, On the origins of ultrahigh hardness and strain gradient plasticity in multi-phase nanocrystalline MoNbTaTiW based refractory high-entropy alloy, Mater. Sci. Eng.-A 812, 141098 (2021).
- 17 S. Yin, J. Ding, M. Asta, and R. O. Ritchie, Ab initio modeling of the energy landscape for screw dislocations in body-centered cubic highentropy alloys, npj Comput. Mater. 6, 110 (2020).
- 18 S. Yin, Y. Zuo, A. Abu-Odeh, H. Zheng, X. G. Li, J. Ding, S. P. Ong, M. Asta, and R. O. Ritchie, Atomistic simulations of dislocation mobility in refractory high-entropy alloys and the effect of chemical short-range order, Nat. Commun. 12, 4873 (2021).
- 19 R. E. Kubilay, A. Ghafarollahi, F. Maresca, and W. A. Curtin, High energy barriers for edge dislocation motion in body-centered cubic high entropy alloys, npj Comput. Mater. 7, 112 (2021).
- 20 F. Maresca, and W. A. Curtin, Mechanistic origin of high strength in refractory BCC high entropy alloys up to 1900K, Acta Mater. 182, 235 (2020)
- 21 S. M. Shaikh, V. S. Hariharan, S. K. Yadav, and B. S. Murty, CALPHAD and rule-of-mixtures: A comparative study for refractory high entropy alloys, Intermetallics 127, 106926 (2020).
- O. N. Senkov, G. B. Wilks, D. B. Miracle, C. P. Chuang, and P. K. Liaw, Refractory high-entropy alloys, Intermetallics 18, 1758 (2010).
- 23 Q. Li, H. Zhang, D. Li, Z. Chen, and Z. Qi, The effect of configurational entropy on mechanical properties of single BCC structural refractory high-entropy alloys systems, Int. J. Refractory Met. Hard Mater. 93, 105370 (2020).
- 24 H. Zhuang, Sudoku-inspired high-Shannon-entropy alloys, Acta Mater. 225, 117556 (2021).
- E. Zhang, Y. Tang, M. Wen, A. Obaied, I. Roslyakova, and L. Zhang, On phase stability of Mo-Nb-Ta-W refractory high entropy alloys, Int. J. Refractory Met. Hard Mater. 103, 105780 (2022).
- W. Brostow, J. P. Dussault, and B. L. Fox, Construction of voronoi polyhedra, J. Comput. Phys. 29, 81 (1978).
- J. Peng, L. Li, F. Li, B. Liu, S. Zherebtsov, Q. Fang, J. Li, N. Stepanov, Y. Liu, F. Liu, and P. K. Liaw, The predicted rate-dependent deformation behaviour and multistage strain hardening in a model heterostructured body-centered cubic high entropy alloy, Int. J. Plast. 145, 103073 (2021).

- 28 S. Plimpton, Fast parallel algorithms for short-range molecular dynamics, J. Comput. Phys. 117, 1 (1995).
- 29 X. W. Zhou, H. N. G. Wadley, R. A. Johnson, D. J. Larson, N. Tabat, A. Cerezo, A. K. Petford-Long, G. D. W. Smith, P. H. Clifton, R. L. Martens, and T. F. Kelly, Atomic scale structure of sputtered metal multilayers, Acta Mater. 49, 4005 (2001).
- 30 J. Li, Q. Fang, B. Liu, and Y. Liu, Transformation induced softening and plasticity in high entropy alloys, Acta Mater. 147, 35 (2018).
- 31 D. Y. Lin, S. S. Wang, D. L. Peng, M. Li, and X. D. Hui, An *n*-body potential for a Zr-Nb system based on the embedded-atom method, J. Phys.-Condens. Matter 25, 105404 (2013).
- 32 K. W. Andrews, Elastic moduli of polycrystalline cubic metals, J. Phys. D-Appl. Phys. 11, 2527 (1978).
- 33 A. Pandey, J. Gigax, and R. Pokharel, Machine learning interatomic potential for high-throughput screening of high-entropy alloys, JOM 74, 2908 (2022).
- 34 F. Körmann, and M. Sluiter, Interplay between lattice distortions, vibrations and phase stability in NbMoTaW high entropy alloys, Entropy 18, 403 (2016).
- 35 Y. Wang, M. Yan, Q. Zhu, W. Y. Wang, Y. Wu, X. Hui, R. Otis, S. L. Shang, Z. K. Liu, and L. Q. Chen, Computation of entropies and phase equilibria in refractory V-Nb-Mo-Ta-W high-entropy alloys, Acta Mater. 143, 88 (2018).
- 36 A. Stukowski, Visualization and analysis of atomistic simulation data with OVITO—the open visualization tool, Model. Simul. Mater. Sci. Eng. 18, 015012 (2010).
- 37 F. Aquistapace, N. Vazquez, M. Chiarpotti, O. Deluigi, C. J. Ruestes, and E. M. Bringa, Atomistic simulations of ductile failure in a b.c.c. high-entropy alloy, High Entropy Alloys Mater. (2022).
- 38 R. A. Romero, S. Xu, W. R. Jian, I. J. Beyerlein, and C. V. Ramana, Atomistic simulations of the local slip resistances in four refractory multi-principal element alloys, Int. J. Plast. 149, 103157 (2022).
- 39 J. M. Cowley, An approximate theory of order in alloys, Phys. Rev. 77, 669 (1950).
- 40 X. B. Feng, J. Y. Zhang, Y. Q. Wang, Z. Q. Hou, K. Wu, G. Liu, and J. Sun, Size effects on the mechanical properties of nanocrystalline NbMoTaW refractory high entropy alloy thin films, Int. J. Plast. 95, 264 (2017).
- 41 P. Rohith, G. Sainath, and V. S. Srinivasan, Effect of size, temperature and strain rate on dislocation density and deformation mechanisms in Cu nanowires, Physica B-Condensed Matter 561, 136 (2019).
- 42 E. Hug, P. A. Dubos, and C. Keller, Temperature dependence and size effects on strain hardening mechanisms in copper polycrystals, Mater. Sci. Eng.-A 574, 253 (2013).
- 43 Z. Wei, D. Wang, X. Yang, C. Wang, G. Chen, and F. Du, From crystalline to amorphous: An effective avenue to engineer highperformance electrode materials for sodium-ion batteries, Adv. Mater. Interfaces 5, 1800639 (2018).
- 44 W. J. Sheng, X. Yang, J. Zhu, C. Wang, and Y. Zhang, Amorphous phase stability of NbTiAlSiN X high-entropy films, Rare Met. 37, 682 (2018).
- 45 Y. Chen, S. W. Reng, J. Peng, and X. B. Liu, Chemical short range order and deformation mechanism of a refractory high entropy alloy HfNbTaZr under nanoindentation: An atomistic study, J. Mater. Res. Tech. 24, 3588 (2023).
- 46 H. Wang, D. Chen, X. An, Y. Zhang, S. Sun, Y. Tian, Z. Zhang, A. Wang, J. Liu, M. Song, S. P. Ringer, T. Zhu, and X. Liao, Deformation-induced crystalline-to-amorphous phase transformation in a CrMnFeCoNi high-entropy alloy, Sci. Adv. 7, eabe3105 (2021).
- 47 D. Choudhuri, B. Gwalani, S. Gorsse, M. Komarasamy, S. A. Mantri, S. G. Srinivasan, R. S. Mishra, and R. Banerjee, Enhancing strength and strain hardenability via deformation twinning in fcc-based high entropy alloys reinforced with intermetallic compounds, Acta Mater. 165, 420 (2019).
- 48 B. Larrouy, P. Villechaise, J. Cormier, and O. Berteaux, Grain boundary-slip bands interactions: Impact on the fatigue crack initiation in a polycrystalline forged Ni-based superalloy, Acta Mater.

- 99, 325 (2015).
- 49 J. M. Monti, E. M. Hopkins, K. Hattar, F. Abdeljawad, B. L. Boyce, and R. Dingreville, Stability of immiscible nanocrystalline alloys in compositional and thermal fields, Acta Mater. 226, 117620 (2022).
- 50 J. Xie, X. P. Chen, Y. Cao, G. J. Huang, and Q. Liu, Microstructure and mechanical properties in Al-Mg-Sc alloy induced by heterodeformation, Mater. Charact. 183, 111622 (2022).
- 51 T. Gao, H. Song, B. Wang, Y. Gao, Y. Liu, Q. Xie, Q. Chen, Q. Xiao, and Y. Liang, Molecular dynamics simulations of tensile response for FeNiCrCoCu high-entropy alloy with voids, Int. J. Mech. Sci. 237, 107800 (2023).
- 52 L. Wang, W. Liu, B. Zhu, W. Chen, F. Zhang, B. Liu, J. Liu, J. Zhou, and Y. Zhao, Influences of strain rate, Al concentration and grain heterogeneity on mechanical behavior of CoNiFeAlxCu1-x highentropy alloys: A molecular dynamics simulation, J. Mater. Res. Tech. 14, 2071 (2021).
- 53 K. Xun, B. Zhang, Q. Wang, Z. Zhang, J. Ding, and E. Ma, Local chemical inhomogeneities in TiZrNb-based refractory high-entropy allovs, J. Mater. Sci. Tech. 135, 221 (2023).
- X. Liu, D. Hua, W. Wang, Q. Zhou, S. Li, J. Shi, Y. He, and H. Wang, Atomistic understanding of incipient plasticity in BCC refractory high entropy alloys, J. Alloys Compd. 920, 166058 (2022).
- 55 L. Li, H. Chen, Q. Fang, J. Li, F. Liu, Y. Liu, and P. K. Liaw, Effects of temperature and strain rate on plastic deformation mechanisms of nanocrystalline high-entropy alloys, Intermetallics 120, 106741 (2020).
- 56 S. Guo, M. Wang, S. Sui, J. Li, H. Chen, X. Hao, X. Zhao, and X. Lin, Research on optimizing strength and ductility of HfNbTaZr dual-phase high-entropy alloy by tuning chemical short-range order, Int. J. Refractory Met. Hard Mater. 108, 105942 (2022).
- 57 F. Wang, G. H. Balbus, S. Xu, Y. Su, J. Shin, P. F. Rottmann, K. E. Knipling, J. C. Stinville, L. H. Mills, O. N. Senkov, I. J. Beyerlein, T. M. Pollock, and D. S. Gianola, Multiplicity of dislocation pathways in a refractory multiprincipal element alloy, Science 370, 95 (2020).
- 58 L. Li, Q. Fang, J. Li, B. Liu, Y. Liu, and P. K. Liaw, Lattice-distortion dependent yield strength in high entropy alloys, Mater. Sci. Eng.-A 784, 139323 (2020).
- 59 K. Yao, and X. Min, Abnormal strain rate strengthening and strain hardening with constitutive modeling in body-centered cubic {332} (113) TWIP titanium alloy, Acta Mater. 226, 117641 (2022).
- 60 J. S. Aristeidakis, and G. N. Haidemenopoulos, Constitutive and transformation kinetics modeling of ε-, α'-Martensite and mechanical twinning in steels containing austenite, Acta Mater. 228, 117757 (2022).
- 61 L. Zhu, H. Ruan, X. Li, M. Dao, H. Gao, and J. Lu, Modeling grain size dependent optimal twin spacing for achieving ultimate high strength and related high ductility in nanotwinned metals, Acta Mater. 59, 5544 (2011).
- 62 J. Li, and A. K. Soh, Modeling of the plastic deformation of nanostructured materials with grain size gradient, Int. J. Plast. 39,

- 88 (2012)
- 63 E. O. Hall, The deformation and ageing of mild steel: III Discussion of results, Proc. Phys. Soc. B 64, 747 (1951).
- 64 Y. Long, X. Liang, K. Su, H. Peng, and X. Li, A fine-grained NbMoTaWVCr refractory high-entropy alloy with ultra-high strength: Microstructural evolution and mechanical properties, J. Alloys Compd. 780, 607 (2019).
- 65 C. Wagner, and G. Laplanche, Effects of stacking fault energy and temperature on grain boundary strengthening, intrinsic lattice strength and deformation mechanisms in CrMnFeCoNi high-entropy alloys with different Cr/Ni ratios, Acta Mater. 244, 118541 (2023).
- 66 J. E. Bailey, and P. B. Hirsch, The dislocation distribution, flow stress, and stored energy in cold-worked polycrystalline silver, Philos. Mag. 5, 485 (1960).
- 67 H. Mecking, and U. F. Kocks, Kinetics of flow and strain-hardening, Acta Metall. 29, 1865 (1981).
- 68 Y. Wei, Scaling of maximum strength with grain size in nanotwinned fcc metals, Phys. Rev. B 83, 132104 (2011).
- 69 C. W. Sinclair, W. J. Poole, and Y. Bréchet, A model for the grain size dependent work hardening of copper, Scripta Mater. 55, 739 (2006).
- 70 J. Li, G. J. Weng, S. Chen, and X. Wu, On strain hardening mechanism in gradient nanostructures, Int. J. Plast. 88, 89 (2017).
- 71 E. Antillon, C. Woodward, S. I. Rao, and B. Akdim, Chemical short range order strengthening in BCC complex concentrated alloys, Acta Mater. 215, 117012 (2021).
- 72 F. Körmann, A. V. Ruban, and M. H. F. Sluiter, Long-ranged interactions in bcc NbMoTaW high-entropy alloys, Mater. Res. Lett. 5, 35 (2017).
- 73 S. Nag, and W. A. Curtin, Effect of solute-solute interactions on strengthening of random alloys from dilute to high entropy alloys, Acta Mater. 200, 659 (2020).
- 74 J. M. Rosenberg, and H. R. Piehler, Calculation of the taylor factor and lattice rotations for bcc metals deforming by pencil glide, Metall. Trans. 2, 257 (1971).
- 75 S. I. Rao, C. Woodward, B. Akdim, E. Antillon, T. A. Parthasarathy, and O. N. Senkov, Estimation of diffusional effects on solution hardening at high temperatures in single phase compositionally complex body centered cubic alloys, Scripta Mater. 172, 135 (2019).
- 76 X. L. Wu, P. Jiang, L. Chen, F. Yuan, and Y. T. Zhu, Extraordinary strain hardening by gradient structure, Proc. Natl. Acad. Sci. USA 111, 7197 (2014).
- 77 H. A. Moreen, R. Taggart, and D. H. Polonis, A model for the prediction of lattice parameters of solid solutions, Metall. Trans. 2, 265 (1971).
- 78 S. Chen, Z. H. Aitken, S. Pattamatta, Z. Wu, Z. G. Yu, D. J. Srolovitz, P. K. Liaw, and Y. W. Zhang, Short-range ordering alters the dislocation nucleation and propagation in refractory high-entropy alloys, Mater. Today 65, 14 (2023).

基于模拟-建模研究化学与温度对难熔高熵合金力学行为 和变形机制的影响

李甲、任思危、刘彬, Peter K. Liaw, 方棋洪

摘要 难熔高熵合金在高温下表现出优异的性能,突破了传统高温合金的工作温度上限. 我们采用原子模拟研究了化学元素分布和温度对等原子比MoNbTaW难熔高熵合金变形机制的影响. 根据微观结构演化,建立了基于微观结构的本构模型,定量评估多种强化机制的贡献. 结果表明,应变硬化后,流动应力随应变呈锯齿状剧烈波动. 由于退火结构的溶质浓度降低,温度升高降低了应变硬化率和流动应力波动幅度. 变形孪晶在变形机制中起着关键作用,能够通过位错基塑性和晶粒中的非晶形核进一步调节局部变形. 有序结构的存在强烈影响了应力和应变分配. 固溶强化和晶界强化对流动应力的贡献很大,孪晶强化对流动压力的贡献很小. 原子模拟和力学模型为深入理解难熔高熵合金变形行为及性能的精确预测提供依据.